



# Particles II

Access the latest eBook →

# 11

Advanced  
Optical Metrology

Particles II



**EVIDENT**  
**OLYMPUS**

**WILEY**

## Impact on Biological Systems and the Environment

This eBook is dedicated to the research of Professor David Wertheim.

In collaboration with various groups, Professor Wertheim uses confocal microscopy to analyse the impact of different types of particles on human health and the environment, with a focus on human health-hazardous particles detected with solid-state nuclear track detectors (SSNTD). Download for free, today.

**EVIDENT**  
**OLYMPUS**

**WILEY**

# Fe–N–C Electrocatalysts with Densely Accessible Fe–N<sub>4</sub> Sites for Efficient Oxygen Reduction Reaction

Yazhou Zhou,\* Guangbo Chen, Qing Wang, Ding Wang, Xiafang Tao, Tierui Zhang, Xinliang Feng,\* and Klaus Müllen\*

This paper is dedicated to Professor Daoben Zhu on the occasion of his 80th birthday

The development of iron and nitrogen co-doped carbon (Fe–N–C) electrocatalysts for the oxygen reduction reaction (ORR) in proton-exchange membrane fuel cells (PEMFCs) is a grand challenge due to the low density of accessible Fe–N<sub>4</sub> sites. Here, an in situ trapping strategy using nitrogen-rich molecules (e.g., melamine, MA) is demonstrated to enhance the amount of accessible Fe–N<sub>4</sub> sites in Fe–N–C electrocatalysts. The melamine molecules can participate in the coordination of Fe ions in zeolitic imidazolate frameworks to form Fe–N<sub>6</sub> sites within precursors. These Fe–N<sub>6</sub> sites are then converted into atomically dispersed Fe–N<sub>4</sub> sites during a pyrolytic process. Remarkably, the Fe–N–C/MA exhibits a high single-atom Fe content (3.5 wt.%), a large surface area (1160 m<sup>2</sup> g<sup>-1</sup>), and a high density of accessible FeN<sub>4</sub> sites (45.7 × 10<sup>19</sup> sites g<sup>-1</sup>). As a result, Fe–N–C/MA shows a much enhanced ORR activity with a half-wave potential of 0.83 V (vs the reversible hydrogen electrode) in a 0.5 M H<sub>2</sub>SO<sub>4</sub> electrolyte solution and a good performance in a PEMFC system with an activity of 80 mA cm<sup>-2</sup> at 0.8 V under 1.0 bar H<sub>2</sub>/air. This work offers a promising approach toward high-performance carbon-based ORR electrocatalysts.

## 1. Introduction

Proton-exchange membrane fuel cells (PEMFCs) represent a sustainable energy conversion technology to overcome problems of global energy consumption and environmental pollution.<sup>[1–3]</sup> The performance of PEMFCs critically relies on the kinetics of the oxygen reduction reaction (ORR) at the cathode.<sup>[4,5]</sup> Up to now, catalysts based on platinum (Pt) group-metal (PGM) are the most efficient materials in PEMFC systems.<sup>[6–8]</sup> However, the prohibitive costs, scarcity, and poor durability of such catalysts seriously hinder their widespread applications and call for PGM-free electrocatalysts as alternatives.<sup>[9]</sup>

Among the PGM-free electrocatalysts, iron and nitrogen co-doped carbon (Fe–N–C) materials are the most promising candidates due to their good activity, abundance, and structural tunability at the


atomic level.<sup>[10–13]</sup> Single atoms of iron coordinated with nitrogen (e.g., Fe–N<sub>4</sub>) moieties in a carbon matrix are commonly recognized as the real active sites for absorbing O<sub>2</sub> and catalyzing the subsequent ORR kinetics.<sup>[14–19]</sup> The Fe–N–C materials can be prepared by the high-temperature pyrolysis of C-, N- and Fe-containing precursors.<sup>[2,20–25]</sup> Nanocrystals of zeolitic imidazolate frameworks (ZIF-8) modified with Fe have proven as highly promising precursors of Fe–N–C electrocatalysts due to their ability to yield Fe–N<sub>4</sub> sites and generate porous nanostructures.<sup>[26–28]</sup> In situ Fe-doping and encapsulation of Fe-containing sources into ZIF-8 nanocrystals are two typical approaches for the preparation of the above precursors.<sup>[29]</sup> For the in situ doping strategy, additional Fe ions, similar to Zn ions, can also chemically bind to 2-methylimidazole ligands upon the formation of Fe-doped ZIF-8 (Fe-ZIF-8).<sup>[30,31]</sup> For encapsulation, Fe-containing precursors (e.g., iron (III) acetylacetonate and ferrocene) are loaded into the ZIF-8 cavities during a hydrothermal process.<sup>[26]</sup> High-temperature pyrolysis (>900 °C) converts the 2-methylimidazole ligands into nitrogen-doped carbons, while the Zn are vaporized and leave abundant micropores, under the formation of porous nanostructures. Fe-containing fragments can be captured by the nitrogen sites to form Fe–N<sub>4</sub> moieties, anchoring on nitrogen-doped graphitic carbons.<sup>[29,31–33]</sup> Unfortunately, due to the massive loss of nitrogen-containing species at high temperatures, the nitrogen content in the doped carbons and the amounts of captured single Fe atoms are always limited, resulting

Dr. Y. Zhou, X. Tao, Prof. K. Müllen  
Max Planck Institute for Polymer Research  
55128 Mainz, Germany  
E-mail: muellen@mpip-mainz.mpg.de

Dr. Y. Zhou, D. Wang, X. Tao  
School of Materials Science and Engineering  
Jiangsu University  
Zhenjiang 212013, P. R. China  
E-mail: yazhou@ujs.edu.cn

Dr. G. Chen, Prof. X. Feng  
Center for Advancing Electronics Dresden (Cfaed)  
and Faculty of Chemistry and Food Chemistry  
Technische Universität Dresden  
01062 Dresden, Germany  
E-mail: xinliang.feng@tu-dresden.de

Q. Wang, Prof. T. Zhang  
Key Laboratory of Photochemical Conversion and Optoelectronic Materials  
Technical Institute of Physics and Chemistry  
Chinese Academy of Sciences  
Beijing 100190, P. R. China

 The ORCID identification number(s) for the author(s) of this article can be found under <https://doi.org/10.1002/adfm.202102420>.

© 2021 The Authors. Advanced Functional Materials published by Wiley-VCH GmbH. This is an open access article under the terms of the Creative Commons Attribution-NonCommercial License, which permits use, distribution and reproduction in any medium, provided the original work is properly cited and is not used for commercial purposes.

DOI: 10.1002/adfm.202102420

in a low density of Fe–N<sub>4</sub> sites (≈0.5 at%) and the formation of inactive Fe-based clusters and/or nanoparticles (NPs).<sup>[30]</sup>

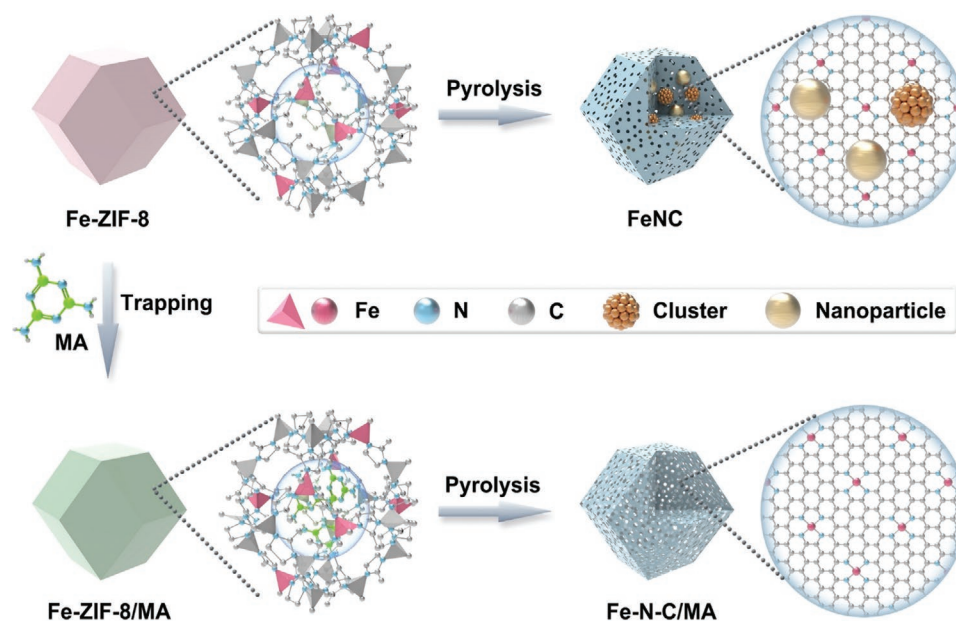
In previous studies, the secondary nitrogen-containing sources, including phenanthroline (Phen), 2-dimethylimidazole (mIm), and 2,4,6-tris(2-pyridyl)-s-triazine, have been introduced into ZIF-8 system to change the coordination environment of Fe ions by a wet impregnation approach.<sup>[34–36]</sup> For example, Tian et al., replaced the ligand of ferrous acetate with Phen to form Fe(Phen)<sub>3</sub> complex on the surface of ZIF-8 particles by wet impregnation followed by drying and planetary ball milling.<sup>[34]</sup> The displacement of ligand enhances metal-ligand coordination strength, thus improving the content of metal-N<sub>x</sub> sites. However, a high amount of nitrogen-containing sources penetrated the inner pores of the ZIF-8 precursor were carbonized to an abundant carbon matrix, resulting in inaccessibility of active sites and low microporosity of catalysts.<sup>[37]</sup> Therefore, these strategies usually involve post-pyrolysis and etching procedures and ammonia activation.<sup>[15,38]</sup>

Herein, we demonstrate an in situ trapping strategy using nitrogen-rich molecules to promote the ORR activity of Fe–N–C electrocatalysts by simultaneously improving the site density and accessibility of Fe–N<sub>4</sub> moieties in hierarchically porous carbons. The nitrogen-rich molecules (e.g., melamine, MA, dicyandiamide, DCD, and Phen) can participate in the coordination of Fe ions upon synthesizing ZIF-8, thereby increasing the content of Fe–N<sub>x</sub> sites e.g., Fe–N<sub>6</sub> in precursors. During thermal carbonization, the Fe–N<sub>x</sub> sites are converted into Fe–N<sub>4</sub> sites inside the porous carbon matrix. The atomically dispersed Fe–N<sub>4</sub> structure is confirmed by aberration-corrected high-angle annular dark-field scanning transmission electron microscopy (AC-HAADF-STEM) study along with X-ray absorption spectroscopy (XAS) analysis. Notably, when using MA as trapping molecules, the resulting Fe–N–C/MA exhibits a high single-atom Fe content of 3.5 wt.%, a large specific surface area of 1160 m<sup>2</sup> g<sup>−1</sup> as well as a high density of

accessible FeN<sub>4</sub> sites of 45.7 × 10<sup>19</sup> sites g<sup>−1</sup>. Benefitting from these attributes, Fe–N–C/MA achieves a high ORR activity with a high half-wave potential (*E*<sub>1/2</sub>) of 0.83 V versus reversible hydrogen electrode (vs RHE) and long-term durability in a 0.5 M H<sub>2</sub>SO<sub>4</sub> electrolyte solution. Moreover, the Fe–N–C/MA demonstrates good performance in PEMFC systems in terms of a high current density of 0.080 A cm<sup>−2</sup> at 0.8 V in H<sub>2</sub>/air condition, which outperforms many reported state-of-the-art Fe–N–C electrocatalysts.<sup>[30,39]</sup>

## 2. Results and Discussion

The synthesis of Fe–N–C/MA is described as an example to highlight the trapping concept, as illustrated in **Scheme 1**. Briefly, the MA molecules were in situ introduced during the synthesis of ZIF-8 by adding iron nitrate nonahydrate, zinc nitrate hexahydrate together with 2-methylimidazole. These MA molecules along with 2-methylimidazole expected to co-coordinate with Fe ions to form high-content Fe–N<sub>x</sub> sites in ZIF-8 (denoted as Fe-ZIF-8/MA). The resulting powder was heated at 1000 °C for 1 h under a flowing Ar atmosphere. The hydrocarbon networks of ZIF-8 were carbonized for the formation of the porous nitrogen-doped carbon matrix, while the Fe–N<sub>x</sub> complexes were converted into atomically dispersed Fe–N<sub>4</sub> sites. A detailed protocol is given in the Supporting Information. As revealed in Figure S1, Supporting Information, the Fe–ZIF-8/MA nanocrystals displayed a defined rhombic dodecahedron shape with a particle size of ≈45 nm. X-ray diffraction (XRD) analysis gave the identical diffraction patterns for ZIF-8, Fe-ZIF-8, and Fe-ZIF-8/MA (Figure S2a, Supporting Information), suggesting that the introduction of melamine did not influence the crystalline structure of the ZIF-8. The Fe K-edge extended X-ray absorption fine structure (EXAFS) was applied to examine the local coordination



**Scheme 1.** Schematic illustration of the synthesis of the Fe–N–C/MA electrocatalyst with a trapping strategy using nitrogen-rich molecules.

geometry of Fe sites in the Fe-ZIF-8/MA precursor. An intense peak at  $\approx 1.5$  Å appeared in the Fe-ZIF-8/MA spectrum, a small shift compared with the first Fe–N shell in the iron phthalocyanine (FePc) reference (Figure S3a, Supporting Information). The first-shell coordination number of the central Fe sites was calculated to be  $\approx 6.5 \pm 0.2$  using EXAFS fitting analysis (Figure S3b and Table S2, Supporting Information), revealing that Fe-ZIF-8/MA likely contained Fe–N<sub>6</sub> complexes. Notably, due to Fe ions being usually coordinated with four 2-methylimidazole ligands to form the Fe–N<sub>4</sub> complexes, the formation of Fe–N<sub>6</sub> sites in the Fe-ZIF-8/MA precursor may be original from the co-coordination of melamine along with 2-methylimidazole ligands.<sup>[40]</sup> The pore size distribution analysis revealed that in addition to 12–14 Å micropores, there was the formation of new and larger 16–19 Å micropores in Fe-ZIF-8/MA precursors, as compared to those of bare Fe-ZIF-8 (Figure S4, Supporting Information), which can be interpreted as defects in the microporous structure due to the above co-coordination process. For comparison, a FeNC reference material was prepared using an identical procedure as for Fe–N–C/MA without the utilization of melamine, and a FeNC/MA sample was synthesized by a wet impregnation approach (see Supporting Information).

The structure of optimized Fe–N–C/MA, made from 200 mg of melamine, was first examined by XRD, scanning electron microscope (SEM), and transmission electron microscopy (TEM) (Figure 1a,b). The XRD pattern of Fe–N–C/MA displayed two broad peaks at 24.3° and 43.7°, corresponding to the (002) and (101) planes of graphitic carbon (Figure S2b, Supporting Information). The product retained the original dodecahedron morphology of Fe-ZIF-8 particles. TEM and high-resolution TEM (HRTEM) images revealed disordered carbon structures with randomly oriented graphitic

domains (Figure 1b,c). Obviously, Fe–N–C/MA contained no Fe-containing clusters and NPs, as confirmed by XRD pattern, HRTEM, and high-angle annular dark-field scanning TEM (HAADF-STEM, Figure 1d) images. Corresponding elemental mapping images (Figure 1e–h) clearly supported the homogeneous distribution of C, N, and Fe elements in the Fe–N–C/MA. Furthermore, the AC-HAADF-STEM image (Figure 1i) indicated that the Fe atoms were atomically dispersed within the graphitic carbons. In sharp contrast, a large amount of NPs with a size of  $\approx 2$  nm appeared in the FeNC, which were identified as Fe<sub>3</sub>C@C by HRTEM and XRD analyses (Figures S5 and S2b, Supporting Information). To understand the critical role of melamine in the synthesis of single-atom Fe catalysts, samples of Fe–N–C/MA-*n* were prepared by changing the content of melamine (*n* corresponds to 100, 150, 200, 250, and 300 mg of melamine). As shown in Figures S6–S10, Supporting Information, along with increased melamine loading from 100 to 200 mg, single Fe atoms were detected (i.e., Fe–N–C/MA-100, Fe–N–C/MA-150, and Fe–N–C/MA-200) without obvious Fe-based clusters and NPs. However, the higher amount of melamine (more than 200 mg) caused the formation of Fe aggregates in the catalysts (Figures S9 and S10, Supporting Information). As shown in Figure S1, Supporting Information, with the increasing amount of melamine, the particle size of ZIF-8 significantly decreased from 150 nm for Fe-ZIF-8 to 30 nm for Fe-ZIF-8/MA-300. This can be ascribed to the fact that the co-coordination of metals by melamine and 2-methylimidazole molecules causes the formation of defects in ZIF-8 and thus limits the growth of nanocrystals. These small particles tend to aggregate during the sintering process at high temperatures so that the pores collapse and can no longer keep Fe atoms from aggregation. In addition, FeNC/MA synthesized by introducing melamine in Fe-ZIF-8 precursors using a wet

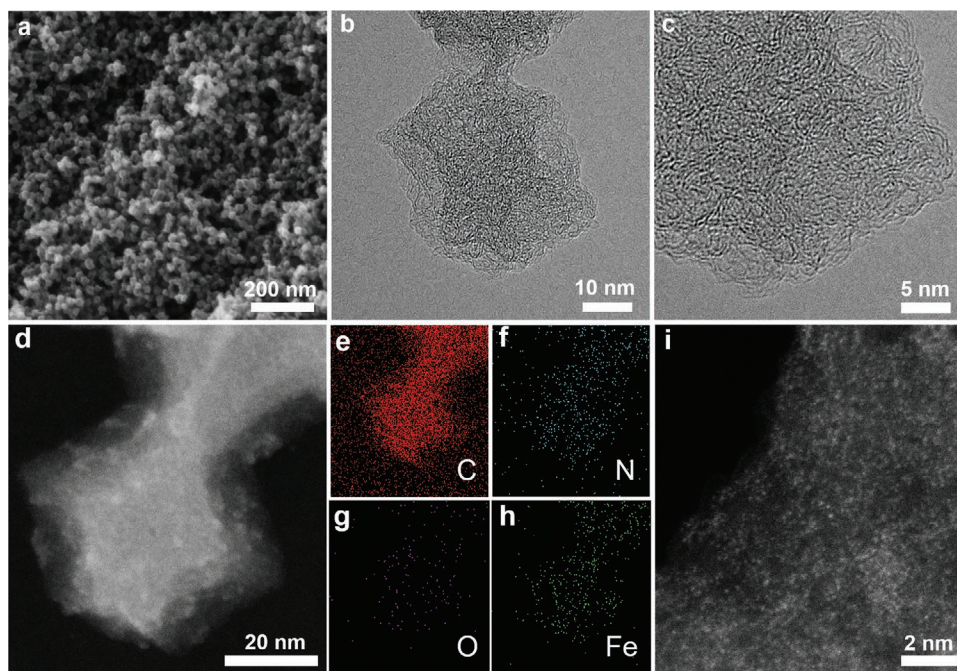


**Figure 1.** a) SEM, b) TEM, c) HRTEM images, d) HAADF-STEM image and corresponding elemental mapping distributions for e) C, f) N, g) O, and h) Fe of the Fe–N–C/MA. i) AC-HAADF-STEM image of the Fe–N–C/MA.

impregnation approach presented abundant Fe NPs, pore collapse, and carbon nanotube structures (Figures S11 and S12, Supporting Information). This proved again the superiority of the trapping strategy for the synthesis of single Fe atom sites. The Fe loading content of optimal Fe–N–C/MA by inductively coupled plasma optical emission spectrometry (ICP-OES) was 3.5 wt.%, which exceeds the values determined for many other Fe–N–C catalysts (Table S3, Supporting Information).<sup>[15,30,41,42]</sup>

The elemental information on the FeNC- and Fe–N–C/MA-surfaces was obtained from X-ray photoelectron spectroscopy (XPS). The XPS survey spectra confirmed the existence of C, N, and Fe in the FeNC and Fe–N–C/MA (Figure S10a, Supporting Information). The Fe–N–C/MA and FeNC exhibited nearly identical high-resolution C 1s spectra (Figure S13b, Supporting Information). The N content in Fe–N–C/MA was as high as 9.1 at%, that is, much higher than that in FeNC (4.9%), as a result of sufficient nitrogen provided by

the added melamine (Table S4, Supporting Information). High-resolution N 1s XPS spectra of the FeNC and Fe–N–C/MA were analyzed in terms of four N species, including pyridinic-N (398.6 eV), graphitic-N (401.2 eV), oxidized N (403–405 eV), and Fe–N (399.5 eV) (Figure S13c, Supporting Information).<sup>[43–44]</sup> The percentage of Fe–N increased from 5.5% for FeNC to 24.9% for Fe–N–C/MA (Table S5, Supporting Information). In comparison to that of FeNC, no metallic Fe peaks were observed in the high-resolution Fe 2p XPS spectrum of Fe–N–C/MA (Figure S13d, Supporting Information).<sup>[45]</sup> The above result also suggests that an additional nitrogen source can capture the Fe for coordination during the pyrolysis, which is responsible for the very high percentage of Fe–N.

The fine atomic structure of Fe single-atom sites in Fe–N–C/MA was investigated by XAS with Fe foil, FeO, Fe<sub>2</sub>O<sub>3</sub>, and FePc serving as standards. XANES determined the oxidation state of Fe atoms in the catalyst, by comparing the edge

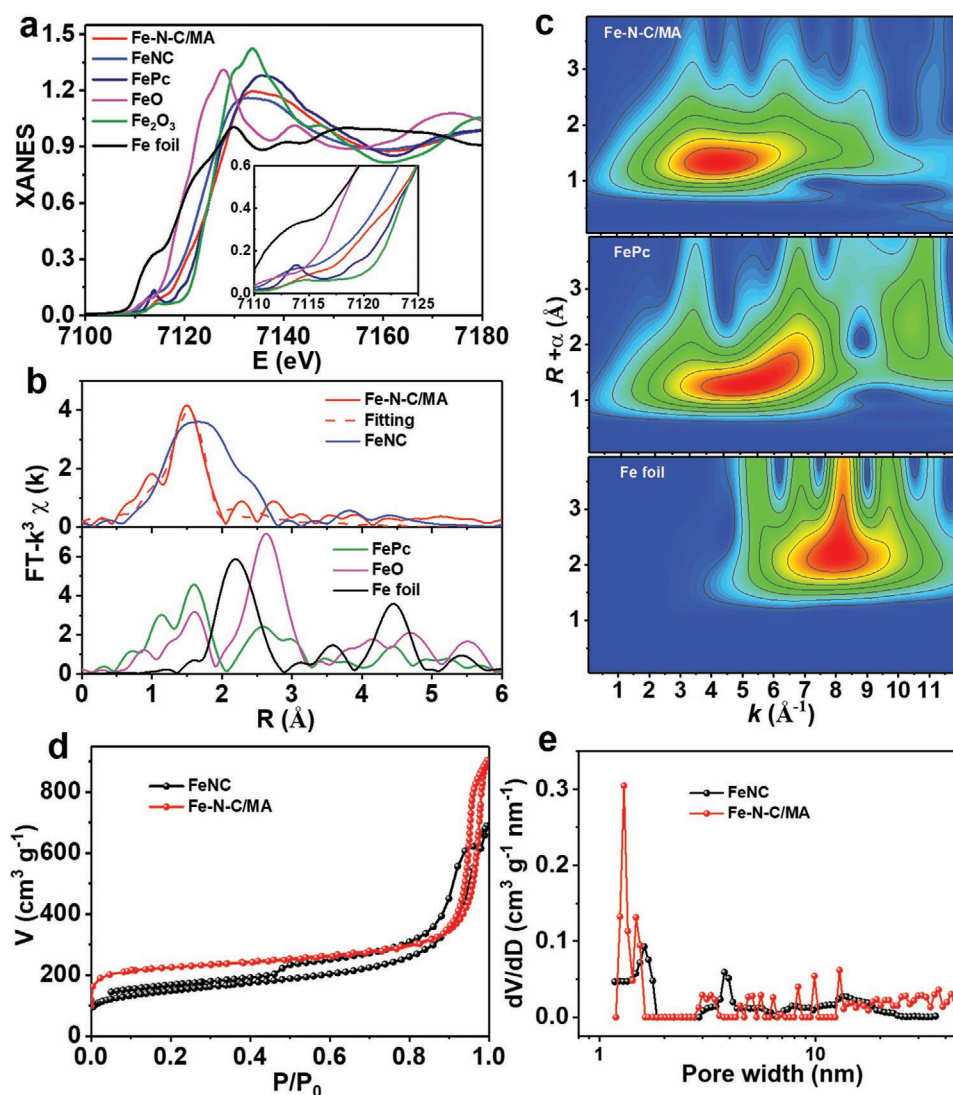


**Figure 2.** a) K-edge XANES spectra, b) Fourier transforms of  $k^3$ -weighted EXAFS of the Fe–N–C/MA, FeNC, and reference samples (FePc, FeO, Fe<sub>2</sub>O<sub>3</sub>, and Fe foil). The dashed line in (b) represents the EXAFS fitting curve of the Fe–N–C/MA. c)  $k^3$ -weighted WT EXAFS spectra of the Fe–N–C/MA, FePc, and Fe foil. d) N<sub>2</sub> adsorption/desorption isotherms and e) the corresponding pore size distributions of the Fe–N–C/MA and FeNC.

position of the samples with that of standard FeO and Fe<sub>2</sub>O<sub>3</sub>. The values of the edge position for all the samples were estimated at 50% absorption. In the Fe K-edge XANES spectra (Figure 2a, inset), the absorption edge of the Fe–N–C/MA was between the standard FeO and Fe<sub>2</sub>O<sub>3</sub>, indicating an oxidation state between +2 and +3.<sup>[46]</sup> The local structure of Fe sites was further uncovered by EXAFS, using both Fourier-transformed (FT) and Wavelet-transformed (WT) methods. At EXAFS R plots (Figure 2b), FeNC exhibited a broad peak in the range of 1–3 Å, which steadily aligned with the Fe–N path at 1.50 Å, Fe–O path at 1.60 Å, and Fe–Fe path at 2.20 Å of FePc, FeO, and Fe foil, respectively,<sup>[11,47]</sup> indicating the co-existence of Fe–N<sub>x</sub> moieties and Fe clusters/NPs with surface oxides. In contrast, Fe–N–C/MA displayed one pronounced peak at ≈1.50 Å, which can be assigned to the Fe–N first coordination shell. The absence of Fe–Fe metallic bonding confirms the atomic dispersion of single Fe atom sites in Fe–N–C/MA (Figure 2b). WT EXAFS is prone to distinguishing the backscattering atoms.<sup>[11]</sup> The WT spectrum of Fe–N–C/MA only revealed one contour intensity maximum at ≈4.50 Å<sup>-1</sup> at k space which was similar to that of FePc, implying again the Fe–N first shell coordination (Figure 2c).<sup>[23,48]</sup> The WT EXAFS analysis indicated that the Fe atoms existed as mononuclear centers without the presence of Fe-derived crystalline structures. EXAFS fitting analysis gave the coordination number and bonding distance of the central Fe atoms with respect to the neighboring scattering atoms in Fe–N–C/MA, providing a first shell Fe–N coordination number and bonding distance of 4.5 ± 0.2 and 1.5 ± 0.2 (Å), respectively (Figure 2b and Table S6, Supporting Information). These results verified that the single Fe atom sites in Fe–N–C/MA possessed a Fe–N<sub>4</sub> configuration, that is, the central Fe atom was coordinated with four nitrogen atoms.

The textural porosities of the FeNC and Fe–N–C/MA-*n* (*n* = 100, 200, and 300) were studied by N<sub>2</sub> adsorption-desorption analysis. As depicted in Figure 2d and Figure S14a, Supporting Information, the hysteresis loops verified the coexistence of micropores, mesopores, and macropores in all samples. Along with increased content of melamine from 100 to 200 mg, Fe–N–C/MA samples exhibited higher Brunauer–Emmett–Teller (BET) surface areas compared to that of FeNC (522 m<sup>2</sup> g<sup>-1</sup>) (Table S7, Supporting Information). The increased BET surface area of Fe–N–C/MA was due to more abundant micropores and mesopores with a broad pore size distribution in comparison to that of FeNC (Figure 2e). The Fe–N–C/MA-200 sample achieved the highest BET surface area of 1160 m<sup>2</sup> g<sup>-1</sup>, comprising a micropore surface area of 815 m<sup>2</sup> g<sup>-1</sup> and an external surface area of 340 m<sup>2</sup> g<sup>-1</sup>. When using higher contents of melamine (300 mg), the BET surface area of Fe–N–C/MA-300 significantly decreased (440 m<sup>2</sup> g<sup>-1</sup>), which was attributed to the carbonization of excessive melamine which blocked the micropores. One concludes that in situ trapping melamine molecules with optimized content can enhance the porosity of the Fe–N–C catalyst.

The importance of incorporating nitrogen-rich molecules was examined by using other sources, for example, DCD and Phen. Electrocatalysts prepared from DCD and Phen (200 mg) were named Fe–N–C/DCD and Fe–N–C/Phen, respectively. The XRD patterns indicated the absence of Fe-containing clusters/NPs in both catalysts (Figure S15, Supporting Information).

The TEM, HRTEM, and AC-HAADF-STEM images of both samples demonstrated that the single Fe atoms were homogeneously distributed within the ZIF-8 derived graphitic carbons (Figure 3a–f). Figure 3g compares the contents of single Fe and specific surface areas of the present Fe–N–C materials and related literature examples. Clearly, these values of our catalysts (i.e., Fe–N–C/MA, Fe–N–C/DCD, and Fe–N–C/Phen) are much higher than those of previously reported state-of-the-art Fe–N–C electrocatalysts made by methods based on ZIF-8,<sup>[11,27,31,49–53]</sup> silica-temple,<sup>[24,54–56]</sup> or ammonia (NH<sub>3</sub>) activation.<sup>[41,57–59]</sup> These findings validate that the incorporation of nitrogen-rich molecules is an efficient and generally applicable method for preparing Fe–N–C electrocatalysts with dense and accessible Fe–N<sub>4</sub> active sites.

The electrocatalytic ORR activities were evaluated using a rotating disk electrode (RDE) technique in an O<sub>2</sub>-saturated 0.5 M H<sub>2</sub>SO<sub>4</sub> electrolyte solution. A commercial Pt/C catalyst (20% Pt, Fuelcellstore) was measured in 0.1 M HClO<sub>4</sub> solution for comparison. All potentials were referenced to RHE. The Fe–N–C/MA fabricated using 200 mg MA exhibited the best ORR performance as revealed by the highest onset potential (*E*<sub>onset</sub>) (defined as the potential at a current density of 0.1 mA cm<sup>-2</sup>) and *E*<sub>1/2</sub> in the ORR polarization plots (Figure S17, Supporting Information). As shown in ORR polarization curves, FeNC exhibited a poor ORR activity with a small onset potential of 0.92 V and a low *E*<sub>1/2</sub> of 0.79 V, attributable to the low density of Fe–N<sub>4</sub> active sites and poor porosity (Figure 4a). By contrast, the Fe–N–C materials offered a substantially improved performance. Particularly, the Fe–N–C/MA, made from 200 mg of MA, manifested the best ORR activity with a high *E*<sub>1/2</sub> of 0.83 V, which was only 20 mV lower than that of benchmark Pt/C catalyst (*E*<sub>1/2</sub>, 0.85 V) and outperforming or equaling those of many state-of-the-art Fe–N–C electrocatalysts (0.7 V < *E*<sub>1/2</sub> < 0.86 V, Table S8, Supporting Information).<sup>[24,31,60–63]</sup> The Tafel slope of Fe–N–C/MA was as low as ≈62 mV dec<sup>-1</sup>, indicating a fast ORR kinetics (Figure S18, Supporting Information). Moreover, Fe–N–C/MA, Fe–N–C/DCD, and Fe–N–C/Phen possessed a much larger kinetic current density (*J*<sub>k</sub>) at 0.85 V than that of FeNC (Figure 4b and Table S8, Supporting Information).

To further quantify the ORR pathway, a rotating ring-disk electrode (RRDE) technique was employed to track the formation of H<sub>2</sub>O<sub>2</sub> during the ORR process. As revealed in Figure 4c, the H<sub>2</sub>O<sub>2</sub> yield of the Fe–N–C/MA was below 2.5% at the potential range from 0.2 to 0.8 V. The electron-transfer number was calculated to be > 3.98, suggesting the desired four-electron ORR process towards the formation of H<sub>2</sub>O. To evaluate its electrochemical durability, Fe–N–C/MA was cycled from 0.6 to 1.0 V at 50 mV s<sup>-1</sup> in an O<sub>2</sub>-saturated 0.5 M H<sub>2</sub>SO<sub>4</sub> electrolyte solution. After 40 000 potential cycles, the *E*<sub>1/2</sub> of Fe–N–C/MA decreased by only 24 mV (Figure 4d), much less than in the case of many reported Fe–N–C catalysts (*E*<sub>1/2</sub> loss, 23–80 mV).<sup>[30,36,64,65]</sup> Active site demetallation and carbon corrosion have been identified as the main reasons for the degradation of Fe–N–C electrocatalysts.<sup>[36,38]</sup> In the AC-HAADF-STEM image, although a majority of single-atom structures were maintained, some Fe clusters become apparent (Figure S19a, Supporting Information). Some catalytic NPs were observed to be agglomerated with severe carbon corrosion (Figure S19b, Supporting Information).

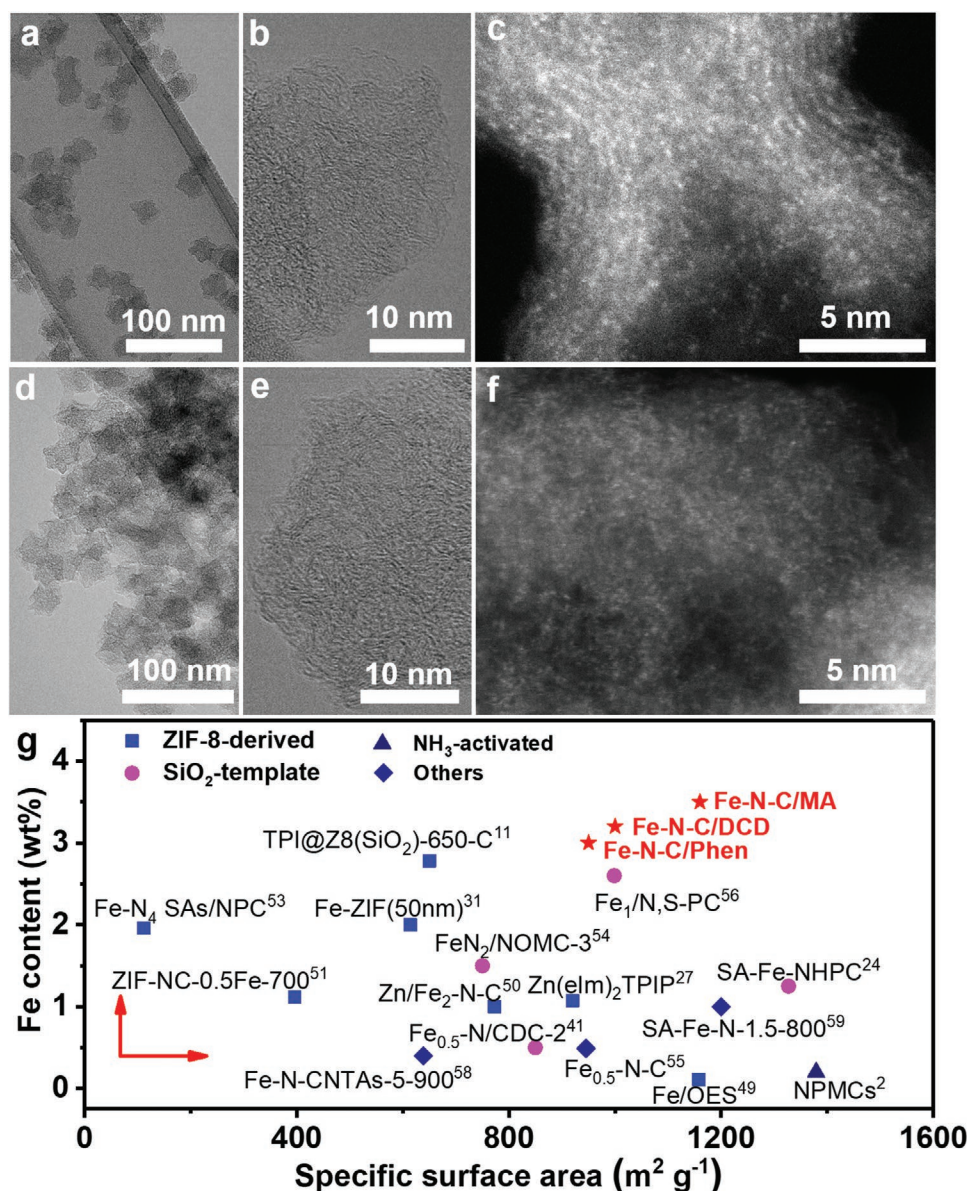


**Figure 3.** a) TEM, b) HRTEM, and c) AC-HAADF-STEM images of the Fe-N-C/DCD. d) TEM, e) HRTEM, and f) AC-HAADF-STEM images of the Fe-N-C/Phen. g) Comparison of specific surface area and content of single Fe atoms comparison for Fe-N-C/MA, Fe-N-C/DCD, Fe-N-C/Phen, and related literature electrocatalysts.

Thus, carbon corrosion could be responsible for breaking the Fe-N coordination, leading to the decomposition of Fe-N<sub>4</sub> sites.

Fe-N-C/MA was then evaluated in PEMFCs as a cathode catalyst in both O<sub>2</sub> and air (Figure 4e) and was compared with reported PGM-free materials (Table S9, Supporting Information). Under 1.0 bar H<sub>2</sub>/O<sub>2</sub> condition, the open-circuit voltage (OCV) reached 0.99 V. At 0.9 V, Fe-N-C generated a current density of 0.019 A cm<sup>-2</sup>, which was approaching the U.S. Department of Energy target value of 0.044 A cm<sup>-2</sup>.<sup>[66]</sup> The corresponding maximum peak power density was 0.47 W cm<sup>-2</sup>. To validate its potential use, Fe-N-C/MA was investigated under H<sub>2</sub>/air conditions (1.0 bar). The OCV was determined to be 0.97 V, which was only 20 mV smaller than that measured in H<sub>2</sub>/O<sub>2</sub>. Fe-N-C/MA was able to generate current densities

of 0.08 and 0.37 A cm<sup>-2</sup> at 0.80 and 0.6 V, respectively. In addition, Fe-N-C/MA assembled PEMFC demonstrated excellent stability with a small current density loss of ≈38% after 120 h at a constant voltage (0.5 V) (Figure S20, Supporting Information), which was superior to previously reported Fe-N-C catalysts (≈50% loss) (Table S9, Supporting Information).<sup>[11,20,27,31,67]</sup>

To gain insight into the effect of physical properties of Fe-N-C catalyst on SD of Fe-N<sub>4</sub>, utilization of active sites, subsequently the ORR activity, we conducted quantitative characterization of the catalyst SD using the in situ electrochemical nitrite poisoning method (Figure S21, Supporting Information).<sup>[11,68]</sup> The catalysts selected for the analyses were FeNC, Fe-N-C/MA-100, Fe-N-C/MA-200, and Fe-N-C/MA-300, with ORR activities decreasing in the order of Fe-N-C/MA-200

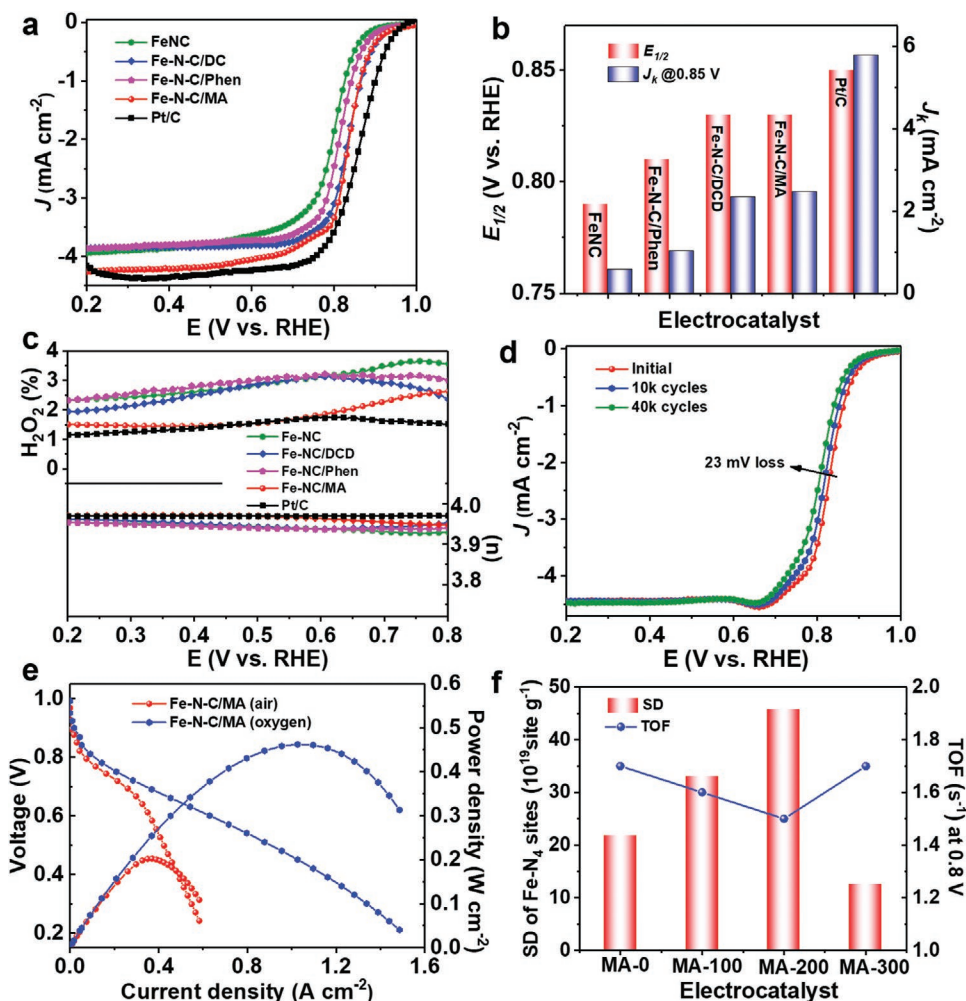


**Figure 4.** a) ORR polarization curves, b)  $E_{1/2}$  and  $J_k$  at 0.85 V, c)  $H_2O_2$  yields and electron-transfer numbers for FeNC, Fe-N-C/MA, Fe-N-C/DCD, Fe-N-C/Phen, and Pt/C electrocatalysts in 0.5 M  $H_2SO_4$  solution with a rotation speed of 900 r.p.m and a potential scan rate of  $10\text{ mV s}^{-1}$ . d) ORR polarization plots of Fe-N-C/MA before and after potential cycling, e) Fuel cell performance of the Fe-N-C/MA measured under 1.0 bar  $H_2/O_2$  and 1.0 bar  $H_2$ /air conditions, f) correlations between SD of Fe-N<sub>4</sub> sites, TOFs, and the content of used melamine in precursors.

> Fe-N-C/MA-100 > FeNC > Fe-N-C/MA-100. The Fe-N-C/MA-200 possessed the highest SD of  $45.7 \times 10^{19}$  site  $g^{-1}$ , which was 2.1-times higher than that of FeNC ( $21.8 \times 10^{19}$  sites  $g^{-1}$ ) (Figure 4f and Table S10, Supporting Information). Then, the correlations between SD, porosity, and ORR performance were examined. As shown in Figure S22a, Supporting Information, we plotted the ORR kinetic current density at 0.85 V as a function of SD. The ORR kinetic activity of a sample was proportional to the SD, indicating a key role of SD in ORR performance. Figure S22b, Supporting Information, showed the correlation between SD and pore structure, revealing that the catalyst with higher microporous surface area was able to host more Fe-N<sub>4</sub> active sites compared to samples with lower microporosity. The results demonstrated that the in situ trapping strategy described here was effective in creating more surface micropores for the accommodation of active Fe-N<sub>4</sub> sites, thereby allowing a high loading of single Fe atoms (3.5 wt.%) and improving ORR activity. The turnover frequencies (TOFs) of all samples were also calculated at 0.8 V based on the stripping charge. Compared to FeNC ( $1.7\text{ s}^{-1}$ ), the Fe-N-C/MA-200 catalyst displayed a lower TOF of  $1.5\text{ s}^{-1}$ , indicating that the average

intrinsic activity of Fe-N<sub>4</sub> active sites in Fe-N-C/MA-200 was slightly decreased. We further determined the utilization ratio of Fe-N<sub>4</sub> sites from the SD and the total content of single Fe atoms (determined by ICP) of a catalyst (Table S10, Supporting Information). Although the utilization ratio of single Fe atoms for Fe-N-C/MA-200 reached 6.0% which was higher than the value of 4.5% reported by Kucernak,<sup>[68]</sup> this demonstrated that abundant Fe-N<sub>4</sub> sites might be located deeper in the micropores or buried under the carbon matrix and, thus, cannot participate in the catalytic ORR. Since micropores play a critical role in the high SD of Fe-N<sub>4</sub> sites while mesopores are responsible for exposing the active sites and enhancing the mass transport,<sup>[69]</sup> it is necessary to further improve the relative abundance of meso- and micropores of Fe-N-C catalyst simultaneously to boost ORR performance.

### 3. Conclusion

In summary, we have demonstrated the fabrication of high-performance Fe-N-C catalysts by a novel in situ trapping



approach using nitrogen-rich molecules followed by a thermal treatment. Nitrogen-rich molecules play a key role in the stabilization of Fe atoms in precursors, resulting in atomically dispersed Fe–N<sub>4</sub> sites in porous carbon with high site density and accessibility. As a result, the as-constructed Fe–N–C catalysts exhibit excellent ORR performance in acidic solutions. Thus, when used as cathode catalyst in PEMFC, Fe–N–C/MA demonstrates good performance under both H<sub>2</sub>/O<sub>2</sub> and H<sub>2</sub>/air conditions, which outperforms those of many reported state-of-the-art Fe–N–C catalysts. Correlations between the Fe–N<sub>4</sub> site density and porosity of catalysts, as well as ORR activity, were established. The present concept along with the findings of this study will stimulate the future exploration of highly active Fe–N–C catalysts for ORR and their application in practical PEMFC systems. The rational design of various single-atom catalysts (Ni, Co, Mn, etc.) will also have an impact on other energy conversion reactions, such as water splitting, N<sub>2</sub> fixation, and CO<sub>2</sub> reduction

## Supporting Information

Supporting Information is available from the Wiley Online Library or from the author.

## Acknowledgements

Y.Z. and G.C. contributed equally to this work. This work was financially supported by the Max Planck Society, Horizon 2020 research and innovation programme GrapheneCore3 (785219 and 881603), DFG for the CRC 1415 (417590517), and the Natural Science Foundation of China (51702129 and 51972150). Y.Z. acknowledges the support from the Postdoctoral Science Foundation (2018M630527). Y.Z. and G.C. thank the China Scholarship Council for financial support (201708320150 and 201606970028). X.T. thanks the scholarship from Jiangsu University. The authors thank Leon Prädél for his XPS measurements.

Open access funding enabled and organized by Projekt DEAL.

## Conflict of Interest

The authors declare no conflict of interest.

## Data Availability Statement

The data that support the findings of this study are available from the corresponding author upon reasonable request.

## Keywords

Fe–N–C catalysts, nitrogen-rich molecules trapping, oxygen reduction reaction, proton exchange membrane fuel cells, site density

Received: April 21, 2021

Revised: May 5, 2021

Published online: June 17, 2021

[1] M. H. Shao, Q. W. Chang, J. P. Dodelet, R. Chenitz, *Chem. Rev.* **2016**, *116*, 3594.

- [2] M. Lefevre, E. Proietti, F. Jaouen, J. P. Dodelet, *Science* **2009**, *324*, 71.
- [3] Z. W. Seh, J. Kibsgaard, C. F. Dickens, I. B. Chorkendorff, J. K. Nørskov, T. F. Jaramillo, *Science* **2017**, *355*, eaad4998.
- [4] H. A. Gasteiger, S. S. Kocha, B. Sompalli, F. T. Wagner, *Appl. Catal., B* **2005**, *56*, 9.
- [5] C. Chen, Y. J. Kang, Z. Y. Huo, Z. W. Zhu, W. Y. Huang, H. L. L. Xin, J. D. Snyder, D. G. Li, J. A. Herron, M. Mavrikakis, M. F. Chi, K. L. More, Y. D. Li, N. M. Markovic, G. A. Somorjai, P. D. Yang, V. R. Stamenkovic, *Science* **2014**, *343*, 1339.
- [6] M. K. Debe, *Nature* **2012**, *486*, 43.
- [7] L. Chong, J. G. Wen, J. Kubal, F. G. Sen, J. X. Zou, J. Greeley, M. Chan, H. Barkholtz, W. J. Ding, D. J. Liu, *Science* **2018**, *362*, 1276.
- [8] Y. Z. Zhou, C. H. Yen, Y. H. Hu, C. M. Wang, X. N. Cheng, C. M. Wai, J. Yang, Y. H. Lin, *J. Mater. Chem. A* **2016**, *4*, 18628.
- [9] A. A. Gewirth, J. A. Varnell, A. M. DiAscro, *Chem. Rev.* **2018**, *118*, 2313.
- [10] G. Wu, K. L. More, C. M. Johnston, P. Zelenay, *Science* **2011**, *332*, 443.
- [11] X. Wan, X. F. Liu, Y. C. Li, R. H. Yu, L. R. Zheng, W. S. Yan, H. Wang, M. Xu, J. L. Shui, *Nat. Catal.* **2019**, *2*, 259.
- [12] N. R. Sahraie, U. I. Kramm, J. Steinberg, Y. J. Zhang, A. Thomas, T. Reier, J. P. Paraknowitsch, P. Strasser, *Nat. Commun.* **2015**, *6*, 8618.
- [13] K. Strickland, M. W. Elise, Q. Y. Jia, U. Tylus, N. Ramaswamy, W. T. Liang, M. T. Sougrati, F. Jaouen, S. Mukerjee, *Nat. Commun.* **2015**, *6*, 7343.
- [14] Y. Mun, S. Lee, K. Kim, S. Kim, S. Lee, J. W. Han, J. Lee, *J. Am. Chem. Soc.* **2019**, *141*, 6254.
- [15] A. Zitolo, V. Goellner, V. Armel, M. T. Sougrati, T. Mineva, L. Stievano, E. Fonda, F. Jaouen, *Nat. Mater.* **2015**, *14*, 937.
- [16] K. J. Chen, K. Liu, P. D. An, H. J. W. Li, Y. Y. Lin, J. H. Hu, C. K. Jia, J. W. Fu, H. M. Li, H. Liu, Z. Lin, W. Z. Li, J. H. Li, Y. R. Lu, T. S. Chan, N. Zhang, M. Liu, *Nat. Commun.* **2020**, *11*, 4173.
- [17] S. Wagner, H. Auerbach, C. E. Tait, I. Martinaiou, S. C. N. Kumar, C. Kubel, I. Sergeev, H. C. Wille, J. Behrends, J. A. Wolny, V. Schunemann, U. I. Kramm, *Angew. Chem., Int. Ed.* **2019**, *58*, 10486.
- [18] X. Li, C. S. Cao, S. F. Hung, Y. R. Lu, W. Cai, A. I. Rykov, S. Miao, S. Xi, H. Yang, Z. Hu, J. Wang, J. Zhao, E. E. Alp, W. Xu, T. S. Chan, H. Chen, Q. Xiong, H. Xiao, Y. Huang, J. Li, T. Zhang, B. Liu, *Chem* **2020**, *6*, 3440.
- [19] T. Marshall-Roth, N. J. Libretto, A. T. Wrobel, K. J. Anderton, M. L. Pegis, N. D. Ricke, T. Van Voorhis, J. T. Miller, Y. Surendranath, *Nat. Commun.* **2020**, *11*, 5283.
- [20] E. Proietti, F. Jaouen, M. Lefevre, N. Larouche, J. Tian, J. Herranz, J. P. Dodelet, *Nat. Commun.* **2011**, *2*, 416.
- [21] H. W. Liang, W. Wei, Z. S. Wu, X. Feng, K. Mullen, *J. Am. Chem. Soc.* **2013**, *135*, 16002.
- [22] Q. Li, T. Y. Wang, D. Havas, H. G. Zhang, P. Xu, J. T. Han, J. Cho, G. Wu, *Adv. Sci.* **2016**, *3*, 1600140.
- [23] H. L. Fei, J. C. Dong, Y. X. Feng, C. S. Allen, C. Z. Wan, B. Voloskiy, M. F. Li, Z. P. Zhao, Y. L. Wang, H. T. Sun, P. F. An, W. X. Chen, Z. Y. Guo, C. Lee, D. L. Chen, I. Shakir, M. J. Liu, T. D. Hu, Y. D. Li, A. I. Kirkland, X. F. Duan, Y. Huang, *Nat. Catal.* **2018**, *1*, 63.
- [24] G. Chen, P. Liu, Z. Q. Liao, F. F. Sun, Y. H. He, H. X. Zhong, T. Zhang, E. Zschech, M. W. Chen, G. Wu, J. Zhang, X. L. Feng, *Adv. Mater.* **2020**, *32*, 1907399.
- [25] Y. Zhou, X. Tao, G. Chen, R. Lu, D. Wang, M. X. Chen, E. Jin, J. Yang, H. W. Liang, Y. Zhao, X. Feng, A. Narita, K. Mullen, *Nat. Commun.* **2020**, *11*, 5892.
- [26] J. Wang, Z. Q. Huang, W. Liu, C. R. Chang, H. L. Tang, Z. J. Li, W. X. Chen, C. J. Jia, T. Yao, S. Q. Wei, Y. Wu, Y. D. Lie, *J. Am. Chem. Soc.* **2017**, *139*, 17281.
- [27] D. Zhao, J. L. Shui, L. R. Grabstanowicz, C. Chen, S. M. Commet, T. Xu, J. Lu, D. J. Liu, *Adv. Mater.* **2014**, *26*, 1093.

- [28] H. Rong, S. Ji, J. Zhang, D. Wang, Y. Li, *Nat. Commun.* **2020**, *11*, 5884.
- [29] Y. J. Chen, S. F. Ji, Y. G. Wang, J. C. Dong, W. X. Chen, Z. Li, R. A. Shen, L. R. Zheng, Z. B. Zhuang, D. S. Wang, Y. D. Li, *Angew. Chem., Int. Ed.* **2017**, *56*, 6937.
- [30] H. Zhang, H. T. Chung, D. A. Cullen, S. Wagner, U. I. Kramm, K. L. More, P. Zelenay, G. Wu, *Energy Environ. Sci.* **2019**, *12*, 2548.
- [31] H. Zhang, S. Hwang, M. Y. Wang, Z. X. Feng, S. Karakalos, L. L. Luo, Z. Qiao, X. H. Xie, C. M. Wang, D. Su, Y. Y. Shao, G. Wu, *J. Am. Chem. Soc.* **2017**, *139*, 14143.
- [32] Q. R. Shi, Y. H. He, X. W. Bai, M. Y. Wang, D. A. Cullen, M. Lucero, X. H. Zhao, K. L. More, H. Zhou, Z. X. Feng, Y. Y. Liu, G. Wu, *Energy Environ. Sci.* **2020**, *13*, 3544.
- [33] J. P. Wang, G. K. Han, L. G. Wang, L. Du, G. Y. Chen, Y. Z. Gao, Y. L. Ma, C. Y. Du, X. Q. Cheng, P. J. Zuo, G. P. Yin, *Small* **2018**, *14*, 1704282.
- [34] J. Tian, A. Morozan, M. T. Sougrati, M. Lefevre, R. Chenitz, J. P. Dodelet, D. Jones, F. Jaouen, *Angew. Chem., Int. Ed.* **2013**, *52*, 6867.
- [35] A. Velazquez-Palenzuela, L. Zhang, L. C. Wang, P. L. Cabot, E. Brillas, K. Tsay, J. J. Zhang, *J. Phys. Chem. C* **2011**, *115*, 12929.
- [36] X. Xie, C. He, B. Li, Y. He, D. A. Cullen, E. C. Wegener, A. J. Kropf, U. Martinez, Y. Cheng, M. H. Engelhard, M. E. Bowden, M. Song, T. Lemmon, X. S. Li, Z. Nie, J. Liu, D. J. Myers, P. Zelenay, G. Wang, G. Wu, V. Ramani, Y. Shao, *Nat. Catal.* **2020**, *3*, 1044.
- [37] Y. F. Ye, F. Cai, H. B. Li, H. H. Wu, G. X. Wang, Y. S. Li, S. Miao, S. H. Xie, R. Si, J. Wang, X. H. Bao, *Nano Energy* **2017**, *38*, 281.
- [38] J. Li, M. T. Sougrati, A. Zitolo, J. M. Ablett, I. C. Oğuz, T. Mineva, I. Matanovic, P. Atanassov, Y. Huang, I. Zenyuk, A. Di Cicco, K. Kumar, L. Dubau, F. Maillard, G. Dražić, F. Jaouen, *Nat. Catal.* **2021**, *4*, 10.
- [39] H. T. Chung, D. A. Cullen, D. Higgins, B. T. Sneed, E. F. Holby, K. L. More, P. Zelenay, *Science* **2017**, *357*, 479.
- [40] J. Gu, C. S. Hsu, L. C. Bai, H. M. Chen, X. L. Hu, *Science* **2019**, *364*, 1091.
- [41] S. Ratso, M. T. Sougrati, M. Kaarik, M. Merisalu, M. Rahn, V. Kisand, A. Kikas, P. Paiste, J. Leis, V. Sammelselg, F. Jaouen, K. Tammeveski, *ACS Appl. Energy Mater.* **2019**, *2*, 7952.
- [42] S. Ratso, M. Kaarik, M. Kook, P. Paiste, J. Aruvali, S. Vlassov, V. Kisand, J. Leis, A. M. Kannan, K. Tammeveski, *Int. J. Hydrogen Energy* **2019**, *44*, 12636.
- [43] Y. Li, Y. Z. Zhou, H. J. Wen, J. Yang, C. Maouche, Q. Q. Liu, Y. Y. Wu, C. Cheng, J. Zhu, X. N. Cheng, *Dalton Trans.* **2018**, *47*, 14992.
- [44] C. Y. Su, Y. Z. Zhou, L. L. Zhang, X. H. Yu, S. Gao, X. J. Sun, C. Cheng, Q. Q. Liu, J. Yang, *Ceram. Int.* **2020**, *46*, 8444.
- [45] Y. Z. Zhou, X. N. Cheng, C. H. Yen, C. M. Wai, C. M. Wang, J. Yang, Y. H. Lin, *J. Power Sources* **2017**, *347*, 69.
- [46] Q. H. Li, W. X. Chen, H. Xiao, Y. Gong, Z. Li, L. R. Zheng, X. S. Zheng, W. S. Yan, W. C. Cheong, R. A. Shen, N. H. Fu, L. Gu, Z. B. Zhuang, C. Chen, D. S. Wang, Q. Peng, J. Li, Y. D. Li, *Adv. Mater.* **2018**, *30*, 1800588.
- [47] D. H. Deng, X. Q. Chen, L. Yu, X. Wu, Q. F. Liu, Y. Liu, H. X. Yang, H. F. Tian, Y. F. Hu, P. P. Du, R. Si, J. H. Wang, X. J. Cui, H. B. Li, J. P. Xiao, T. Xu, J. Deng, F. Yang, P. N. Duchesne, P. Zhang, J. G. Zhou, L. T. Sun, J. Q. Li, X. L. Pan, X. H. Bao, *Sci. Adv.* **2015**, *1*, e1500462.
- [48] S. Ratso, A. Zitolo, M. Kaarik, M. Merisalu, A. Kikas, V. Kisand, M. Rahn, P. Paiste, J. Leis, V. Sammelselg, S. Holdcroft, F. Jaouen, K. Tammeveski, *Renewable Energy* **2021**, *167*, 800.
- [49] C. C. Hou, L. L. Zou, L. M. Sun, K. X. Zhang, Z. Liu, Y. W. Li, C. X. Li, R. Q. Zou, J. H. Yu, Q. Xu, *Angew. Chem., Int. Ed.* **2020**, *59*, 7384.
- [50] J. L. Xue, Y. S. Li, J. Hu, *J. Mater. Chem. A* **2020**, *8*, 7145.
- [51] J. Z. Li, H. G. Zhang, W. Samarakoon, W. T. Shan, D. A. Cullen, S. Karakalos, M. J. Chen, D. M. Gu, K. L. More, G. F. Wang, Z. X. Feng, Z. B. Wang, G. Wu, *Angew. Chem., Int. Ed.* **2019**, *58*, 18971.
- [52] Q. Liu, X. Liu, L. Zheng, J. Shui, *Angew. Chem., Int. Ed.* **2018**, *57*, 1204.
- [53] Y. Pan, S. J. Liu, K. A. Sun, X. Chen, B. Wang, K. L. Wu, X. Cao, W. C. Cheong, R. G. Shen, A. J. Han, Z. Chen, L. R. Zheng, J. Luo, Y. Lin, Y. Q. Liu, D. S. Wang, Q. Peng, Q. Zhang, C. Chen, Y. D. Li, *Angew. Chem., Int. Ed.* **2018**, *57*, 8614.
- [54] H. J. Shen, E. Gracia-Espino, J. Y. Ma, H. D. Tang, X. Mamat, T. Wagberg, G. Z. Hu, S. J. Guo, *Nano Energy* **2017**, *35*, 9.
- [55] S. H. Lee, J. Kim, D. Y. Chung, J. M. Yoo, H. S. Lee, M. J. Kim, B. S. Mun, S. G. Kwon, Y. E. Sung, T. Hyeon, *J. Am. Chem. Soc.* **2019**, *141*, 2035.
- [56] K. Wu, X. Chen, S. Liu, Y. Pan, W.-C. Cheong, W. Zhu, X. Cao, R. Shen, W. Chen, J. Luo, W. Yan, L. Zheng, Z. Chen, D. Wang, Q. Peng, C. Chen, Y. Li, *Nano Res.* **2018**, *11*, 6260.
- [57] S. Ratso, N. R. Sahraie, M. T. Sougrati, M. Kaarik, M. Kook, R. Saar, P. Paiste, Q. Y. Jia, J. Leis, S. Mukerjee, F. Jaouen, K. Tammeveski, *J. Mater. Chem. A* **2018**, *6*, 14663.
- [58] C. Z. Zhu, S. F. Fu, J. H. Song, Q. R. Shi, D. Su, M. H. Engelhard, X. L. Li, D. D. Xiao, D. S. Li, L. Estevez, D. Du, Y. H. Lin, *Small* **2017**, *13*, 1603407.
- [59] Z. P. Miao, X. M. Wang, M. C. Tsai, Q. Q. Jin, J. S. Liang, F. Ma, T. Y. Wang, S. J. Zheng, B. J. Hwang, Y. H. Huang, S. J. Guo, Q. Li, *Adv. Energy Mater.* **2018**, *8*, 1801226.
- [60] Y. J. Chen, S. F. Ji, S. Zhao, W. X. Chen, J. C. Dong, W. C. Cheong, R. A. Shen, X. D. Wen, L. R. Zheng, A. I. Rykov, S. C. Cai, H. L. Tang, Z. B. Zhuang, C. Chen, Q. Peng, D. S. Wang, Y. D. Li, *Nat. Commun.* **2018**, *9*, 5422.
- [61] X. L. Zhao, X. X. Yang, M. Y. Wang, S. Hwang, S. Karakalos, M. J. Chen, Z. Qiao, L. Wang, B. Liu, Q. Ma, D. A. Cullen, D. Su, H. P. Yang, H. Y. Zang, Z. X. Feng, G. Wu, *Appl. Catal., B* **2020**, *279*, 119400.
- [62] H. Shen, E. Gracia-Espino, J. Ma, K. Zang, J. Luo, L. Wang, S. Gao, X. Mamat, G. Hu, T. Wagberg, S. Guo, *Angew. Chem., Int. Ed.* **2017**, *56*, 13800.
- [63] L. Yang, D. J. Cheng, X. F. Zeng, X. Wan, J. L. Shui, Z. H. Xiang, D. P. Cao, *Proc. Natl. Acad. Sci. U. S. A.* **2018**, *115*, 6626.
- [64] G. Wu, M. A. Nelson, N. H. Mack, S. G. Ma, P. Sekhar, F. H. Garzon, P. Zelenay, *Chem. Commun.* **2010**, *46*, 7489.
- [65] J. Z. Li, M. J. Chen, D. A. Cullen, S. Hwang, M. Y. Wang, B. Y. Li, K. X. Liu, S. Karakalos, M. Lucero, H. G. Zhang, C. Lei, H. Xu, G. E. Sterbinsky, Z. X. Feng, D. Su, K. L. More, G. F. Wang, Z. B. Wang, G. Wu, *Nat. Catal.* **2018**, *1*, 935.
- [66] Y. Jin, H. Wang, J. Li, X. Yue, Y. Han, P. K. Shen, Y. Cui, *Adv. Mater.* **2016**, *28*, 3785.
- [67] Q. T. Liu, X. F. Liu, L. R. Zheng, J. L. Shui, *Angew. Chem., Int. Ed.* **2018**, *57*, 1204.
- [68] D. Malko, A. Kucernak, T. Lopes, *Nat. Commun.* **2016**, *7*, 13285.
- [69] G. Chen, T. Wang, P. Liu, Z. Liao, H. Zhong, G. Wang, P. Zhang, M. Yu, E. Zschech, M. Chen, J. Zhang, X. Feng, *Energy Environ. Sci.* **2020**, *13*, 2849.